A Rapid Synthesis of Mesoporous Mn_2O_3 Nanoparticles for Supercapacitor Applications

You-Hyun Son [1], Phuong T. M. Bui [1], Ha-Ryeon Lee [1], Mohammad Shaheer Akhtar [1,2,*], Deb Kumar Shah [1] and O-Bong Yang [1,2,*]

[1]   School of Semiconductor and Chemical Engineering & Solar Energy Research Center, Chonbuk National University, Jeonju 54896, Korea; youheun94@jbnu.ac.kr (Y.-H.S.); missbui0504@gmail.com (P.T.M.B.); haryeonlee@jbnu.ac.kr (H.-R.L.); dkshah149@jbnu.ac.kr (D.K.S.)

[2]   New and Renewable Energy Materials Development Center (NewREC), Chonbuk National University, Jeonbuk 54896, Korea

*   Correspondence: shaheerakhtar@jbnu.ac.kr (M.S.A.); obyang@jbnu.ac.kr (O-B.Y.)

Abstract: Mn_2O_3 nanomaterials have been recently composing a variety of electrochemical systems like fuel cells, supercapacitors, etc., due to their high specific capacitance, low cost, abundance and environmentally benign nature. In this work, mesoporous Mn_2O_3 nanoparticles (NPs) were synthesized by manganese acetate, citric acid and sodium hydroxide through a hydrothermal process at 150 °C for 3 h. The synthesized mesoporous Mn_2O_3 NPs were thoroughly characterized in terms of their morphology, surfaces, as well as their crystalline, electrochemical and electrochemical properties. For supercapacitor applications, the synthesized mesoporous Mn_2O_3 NP-based electrode accomplished an excellent specific capacitance (C_{sp}) of 460 F·g^{-1} at 10 mV·s^{-1} with a good electrocatalytic activity by observing good electrochemical properties in a 6 M KOH electrolyte. The excellent C_{sp} might be explained by the improvement of the surface area, porous surface and uniformity, which might favor the generation of large active sites and a fast ionic transport over the good electrocatalytic surface of the Mn_2O_3 electrode. The fabricated supercapacitors exhibited a good cycling stability after 5000 cycles by maintaining ~83% of C_{sp}.

Keywords: Mn_2O_3; mesoporous materials; electrochemical characterizations; electrode; supercapacitors

1. Introduction

A popular electrochemical energy-storage system, the supercapacitor has been a well-explored device as a heartening energy storage because of its high-power density, marvelous cycling and fast charge-discharge mechanisms [1–4]. Supercapacitors, on the basis of their charge-storage process, are classified into two types: i) double layer electrochemical capacitors (EDLCs), built from the electrode and electrolyte interface for the ions adsorption-desorption, and ii) the electrode materials-governed faradaic reaction-based pseudocapacitors [5–7]. In comparison with the EDLCs, the pseudocapacitors have exhibited a fast and desirable reversible redox reaction that promotes an excellent charging and discharging process, resulting in the enhancement of the charge storage capacities. In addition, pseudocapacitors display a highly competent storage device for rechargeable batteries owing to their fast energy harvesting, high energy and high-power delivery [8–10]. In supercapacitors, the active electrodes are normally prepared with carbon-based materials, conducting polymers, and a variety of transition metal oxide materials [11–14]. In recent years, transition metal oxides, such as RuO_2, MnO_2, Mn_3O_4, NiO, Nb_2O_5, V_2O_5, CoO_x, MoO_3, and TiO_2, have been frequently applied in preparing

an effective electrode for supercapacitors due to their abundance in nature, inexpensive nature and extraordinary redox activity [13–21].

Apart from other transition metal oxides, the manganese-based oxides (MnO_x) and their derivatives, like MnO_2, Mn_2O_3, and Mn_3O_4, are popularly used as electrode materials in supercapacitors because they have a non-toxic nature, good structural flexibility and excellent chemical and physical stability in various electrolytes [22]. In particular, Mn_2O_3 materials as anode materials in lithium ion batteries have shown a high capacity and demonstrate a theoretically high specific capacity of ~1018 mAh/g, while also exhibiting a high specific capacitance [23]. Until now, the Mn_2O_3 materials-based electrodes in supercapacitors have been less explored and could be expected to have a high capacity and storage properties as they show an excellent environment compatibility and a resistance in acidic/alkaline electrolytes. Numerous efforts have been made to improve the performance of Mn_2O_3-based electrodes by adopting various modifications, such as chemical modifications [24], the incorporation of high surface-area conductive materials [25,26] and nanostructure fabrication [24,27]. Therefore, the synthesis of Mn_2O_3 materials with a controlled size, morphology and density through a cost-effective, simple and environment friendly method could be potentially sound [28,29]. It is expected that mesoporous Mn_2O_3 nanomaterials might show a surface that is fruitful for fast ion transportation in electrochemical supercapacitors [30].

In this work, a rapid and low temperature hydrothermal process was used to synthesize well-crystalline mesoporous Mn_2O_3 materials that were successfully applied as electro-active materials for a pseudosupercapacitor. The prepared mesoporous Mn_2O_3 materials-based electrode exhibits a high specific capacitance of 460 $F \cdot g^{-1}$ at a scan rate of 10 $mV \cdot s^{-1}$, with a good cycling stability after 5000 cycles.

2. Materials and Methods

In a typical synthesis, a mixture of 1 g of manganese acetate ($Mn(CH_3CO_2)_2$, Sigma-Aldrich, Saint Louis, MO, USA) and 0.5 g citric acid (Samchun Chemicals, Seoul, Korea) was dissolved in 100 mL of deionized (DI) water. Using an aqueous 5 M NaOH solution, the pH of the reaction mixture was adjusted to pH ~10 as the solution color changed from bright brown to dark brown. The hydrothermal process was carried out by transferring the reaction mixture into a Teflon beaker that was tightly sealed. Finally, a temperature of 150 °C was maintained for 3 h. After cooling down the autoclave, the obtained precipitates were collected by filtration, washed several times with DI water and with ethanol. The collected precipitates were dried in an oven overnight at 80 °C, and finally the obtained black powder was calcined at 500 °C in 1 h to remove other impurities.

For the electrochemical supercapacitor application, the synthesized mesoporous Mn_2O_3 electrode was prepared by mixing 85 wt.% Mn_2O_3 powders, 10 wt.% carbon black (Super P, Venatech, Seoul, South Korea), 3 wt.% carboxyl methyl cellulose (CMC, Sigma-Aldrich) and 2 wt.% polytetrafluoroethylene (PTFE, TCI chemical, Tokyo, Japan) in DI water to obtain a paste that was spread over the Ni foam using a glass rod via the rolling method. Afterward, the mesoporous Mn_2O_3-coated Ni foam electrodes were dried in the oven at 80 °C for 20 min to remove the solvent. For the electrochemical measurement, a three-electrode system, comprised of Mn_2O_3-coated Ni foam as the working electrode, Pt wire as the counter electrode and Ag/AgCl as the reference electrode, was used, and a cyclicvoltametric measurement (VersaSTAT4, AMETEK, Inc., Berwyn, PA, USA) was performed in an aqueous 6 M KOH electrolyte. All cyclicvoltametry (CV) measurements were observed at different scan rates ranging from 10 to 500 $mV \cdot s^{-1}$ in the voltage range of 0 to 1.0 V. A potentiostat/galvanostat (VersaSTAT4, AMETEK, Inc.) was used to analyze the electrochemical impedance spectroscopy (EIS) of the fabricated supercapacitor, based on the mesoporous Mn_2O_3 electrode, with a frequency ranging from 0.1 Hz to 1 MHz. For the calculation of C_{sp}, the mass loading of the mesoporous Mn_2O_3 on the electrode was ~0.001 g.

3. Results and Discussion

The morphological features of the synthesized mesoporous Mn_2O_3 materials were analyzed by field emission scanning electron microscopy (FESEM, Hitachi S-4800, Tokyo, Japan) and transmission electron microscopy (TEM, JEM-ARM200F, JEOL, Peabody, MA, USA) observations. Figure 1a,b shows the FESEM images of the synthesized mesoporous Mn_2O_3 materials at low and high magnifications. The spherical small particles, which are highly uniform, are visible in Figure 1a. From FESEM observations, it is difficult to identify the porosity of the synthesized materials. At a high magnification mode (Figure 1b), the obtained particles possess highly porous structures with average sizes of 10–30 nm. A similar observation for synthesized mesoporous Mn_2O_3 materials was detected in the TEM and high-resolution transmission electron microscopy (HRTEM) analyses, as shown in Figure 1c,d. As seen in Figure 1c, the synthesized Mn_2O_3 materials show a similar spherical shape, with a few semi-spherical particles having average particle sizes of ~10–30 nm. A close look at Figure 1c shows that the porosity of the synthesized Mn_2O_3 materials might be defined by the presence of visible voids over the particle surfaces. As reported earlier [31], these voids in materials may be a detrimental factor of the porosity of the materials. The HRTEM image is shown in Figure 1d; it expresses clear lattice fringes from when the measurement was focused on one particle from Figure 1c. From the HRTEM image, the interplanar distance between two lattice fringes is estimated to be ~0.27 nm, which is well-indexed to the (222) plane of Mn_2O_3 [32].
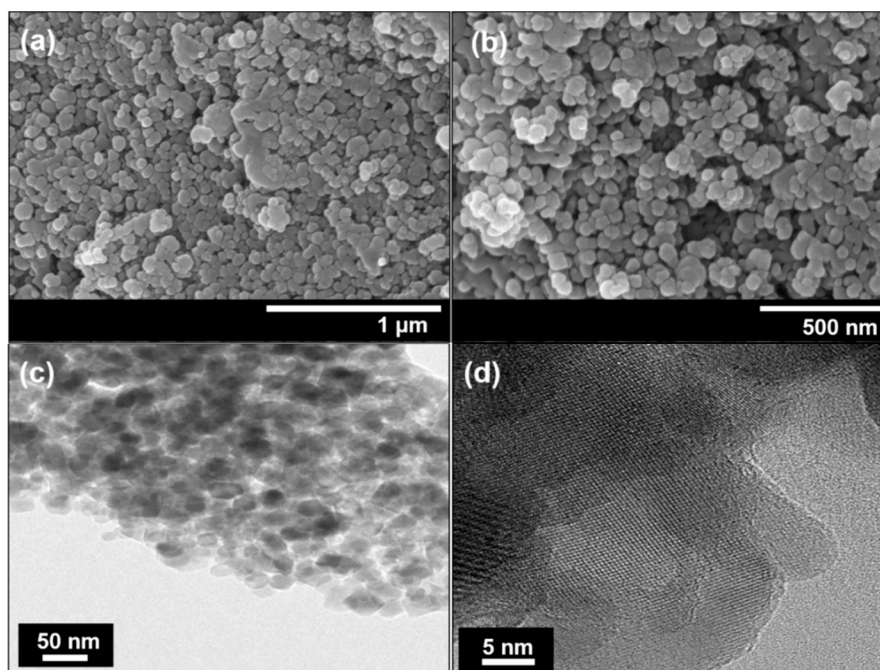

Figure 1. The (**a**,**b**) FESEM, (**c**) TEM and (**d**) HRTEM images of the synthesized mesoporous Mn_2O_3 materials.

The crystalline behavior and crystal planes of the synthesized mesoporous Mn_2O_3 materials were determined via a wide-angle X-ray diffraction (XRD, PANalytical, Malvern, United Kingdom) measurement, as shown in Figure 2. The well-defined diffraction peaks at 18.9°, 23.1°, 33.1°, 38.2°, 45.2°, 47.3°, 49.5°, 55.1° and 65.8° are associated to (200), (211), (222), (400), (332), (422), (431), (440) and (622) planes, respectively. All of the obtained diffraction peaks are assigned perfectly to the Bixbyite crystal phase α-Mn_2O_3, with JCPDS no. 41-1442 and space group Ia3, lattice constants $a = b = c = 9.4091$ Å,

$\alpha = \beta = \gamma = 90°$. To estimate the crystallite sizes (*CS*) of the synthesized mesoporous Mn_2O_3 materials, the Debey–Scherrer equation was used [33]:

$$CS = \frac{0.95 \times \lambda}{\beta \cos(\theta)} \qquad (1)$$

where β is the breadth of the observed diffraction line at its half-intensity maximum, *K* is the so-called shape factor, which usually takes a value of about 0.9, and λ is the wavelength of the X-ray source used in the XRD. By taking the maximum diffraction peak of (222), the crystallite size of the mesoporous Mn_2O_3 materials is found to be 28 nm, which is very close to the FESEM and TEM results.
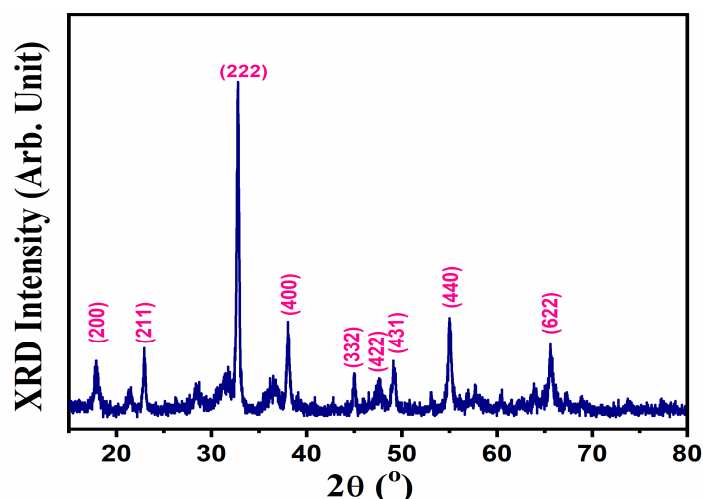

Figure 2. The XRD patterns of the synthesized mesoporous Mn_2O_3 materials.

Figure 3 shows the infrared (IR, Nicolet, IR300, Thermo Fisher Scientific, Waltham, MA, USA) and Raman spectroscopic studies (Raman microscope, Renishaw, UK) that define the structural properties of the synthesized mesoporous Mn_2O_3 materials. As seen in Figure 3a, two sharp IR bands are observed at 610 and at 520 cm^{-1}, assigning the stretching vibrations of Mn–O units and the asymmetric Mn–O–Mn stretching vibration, respectively [34]. Other IR bands at 1640 and 3343 cm^{-1} are detected, related to –OH and the water species from atmospheric moisture. It is believed that the observation of the IR bands at 520 and 610 cm^{-1} clearly reveals the formation of Mn_2O_3 without other impurities. Figure 3b depicts the Raman scattering spectroscopy of the synthesized mesoporous Mn_2O_3 materials. The mesoporous Mn_2O_3 NPs present a strong Raman band at 651 cm^{-1}, including with two weak Raman bands at 268 and at 175.0 cm^{-1}. The strong Raman band at 651 cm^{-1} represents the characteristic of the Mn_2O_3 along with the space group Ia3 structure [35], suggesting the typical symmetric stretching Mn–O–Mn bridge in Mn_2O_3. The main Raman band is well-matched with the reported literature of Mn_2O_3 [35]. Additionally, two weak Raman bands at ~268 and ~175 are assigned to the out-of-plane bending modes of Mn_2O_3 and the asymmetric stretching of the bridge oxygen species (Mn–O–Mn) [36], respectively.

To explain the thermal and structural properties, a thermal gravimetric analysis (TGA, Thermal analyzer, TA Instrument Ltd., New Castle, DE, USA) was performed for the synthesized mesoporous Mn_2O_3 materials, as displayed in Figure 4a,b. As seen in Figure 4b, four decomposition temperatures were visibly identified in the range of 25 to 800 °C. After 500 °C, the subsequent weight loss of ~1.5% that started from 500 to 600 °C is ascribed to the thermal decomposition of Mn_2O_3 to MnO, a decomposition that is usual in metal oxides. In the beginning, the synthesized mesoporous Mn_2O_3 materials were recorded as having a very small weight loss of ~0.5% up to 500 °C, which usually occurs via the removal of water/moisture from the sample. This suggests that the synthesized mesoporous Mn_2O_3 NPs exhibit a remarkably good stability with a high crystalline nature of Mn_2O_3.
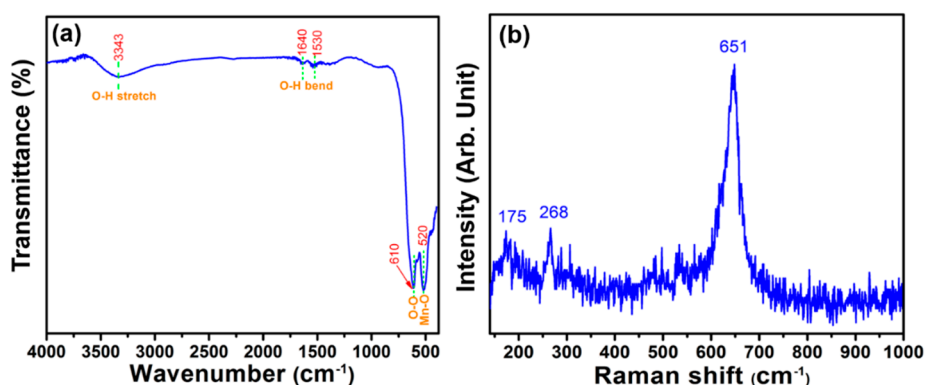
Figure 3. The (**a**) Fourier-transform infrared spectroscopy (FTIR) and (**b**) Raman spectrum of the synthesized mesoporous Mn_2O_3 materials.

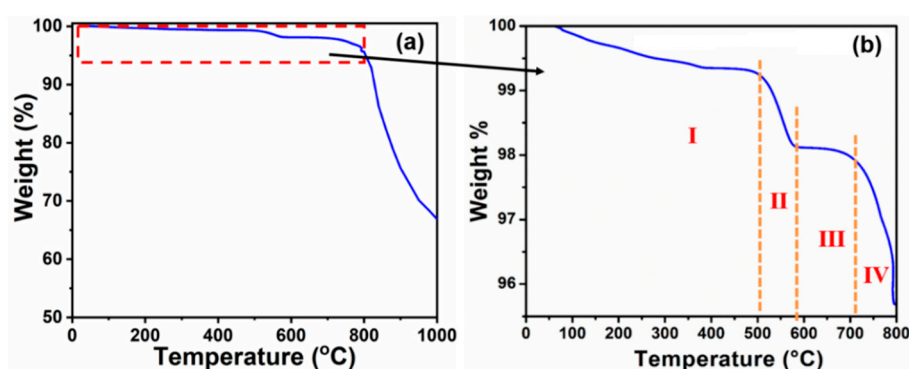**Figure 4.** (**a**,**b**) TGA plot of the synthesized mesoporous Mn_2O_3 materials.

The synthesized mesoporous Mn_2O_3 materials were further characterized in terms of their composition and the oxidation states of the elements using an X-ray photoelectron spectroscopy (XPS, AXISNOVA CJ109, Kratos Inc., Manchester, UK) analysis. Figure 5a shows the survey XPS spectrum of the synthesized mesoporous Mn_2O_3 materials, revealing Mn 2*p*, Mn 3*s* and O 1*s* with weak C 1*s* peaks. The high-resolution Mn 2*p* XPS spectra of the synthesized mesoporous Mn_2O_3 materials is shown in Figure 5b and demonstrates doublet binding energies at 641.0 (Mn 2*p*$_{3/2}$) and 652.8 eV (Mn 2*p*$_{1/2}$). It is noted that the doublet Mn 2*p*, with an estimated spin–orbit splitting value of 11.8 eV, is nearly the same as the values reported for Mn_2O_3 [37]. Additionally, Figure 5c displays the high-resolution Mn 3*s* with characteristic doublet binding energies at 88.8 and 83.5 eV for Mn_2O_3. From the Mn 3*s* XPS, the peak separation for the doublet binding energies are ~5.3 eV, which is very close to the peak separation of Mn 3*s* in Mn_2O_3 [38], which again implies the formation of Mn_2O_3. Figure 5d depicts the high-resolution O 1*s* XPS spectrum. The two binding energies at 528.9 and 530.7 eV are normally related to oxygen O^{2-} in the lattice of Mn–O–Mn, indicating the formation of Mn_2O_3. Therefore, the XPS analysis implied the formation of a pure Mn_2O_3 form without any other oxide impurities [39].

The surface and porous behavior of the synthesized mesoporous Mn_2O_3 materials have been elucidated by analyzing the nitrogen (N_2) adsorption-desorption isotherms and BET surface analyzer, as shown Figure 6. The N_2 adsorption-desorption isotherms (Figure 6a) present a regular type IV isotherm with a small hysteresis in the relative pressure (p/p_0) range of 0.75–0.9, which clearly imitated the mesoporous characteristic of materials. Figure 6b shows how the pore size distribution (*d*) of the mesoporous Mn_2O_3 materials was recorded in the range of 10–30 nm, which is the case for mesoporous materials. Using a Brunauer-Emmett-Teller (BET) surface analysis, the specific surface area (*s*) for the synthesized mesoporous Mn_2O_3 materials was determined to be 76.9 $m^2 \cdot g^{-1}$. Thus, the synthesized Mn_2O_3 materials are mesoporous in nature which could provide a larger surface area for the high ion diffusion of ions in the electrolyte for high-performance supercapacitors.
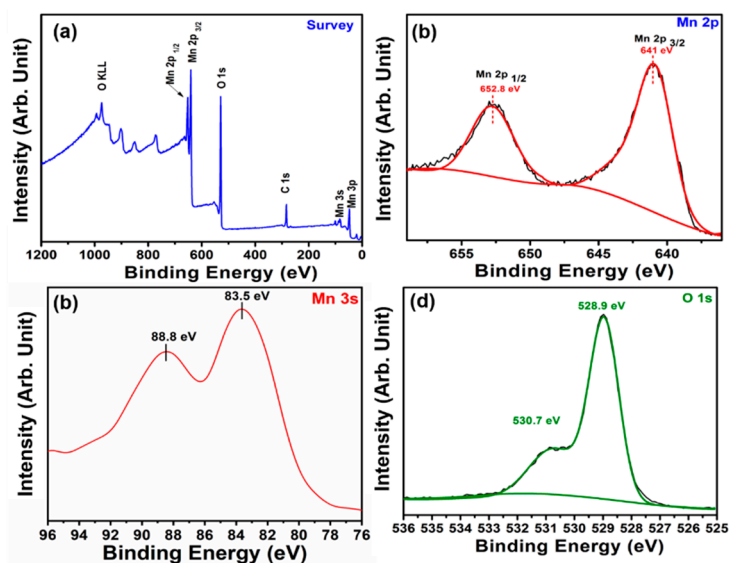
Figure 5. (**a**) Survey, (**b**) high resolution Mn 2*p*, (**c**) Mn 3*s*, and (**d**) O 1*s* XPS of the synthesized mesoporous Mn_2O_3 materials.
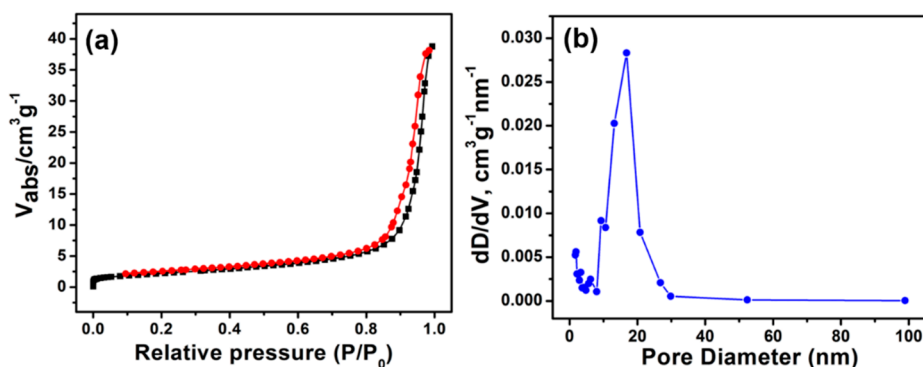

Figure 6. The (**a**) N_2 adsorption-desorption isotherm and (**b**) pore size distribution plot of the synthesized mesoporous Mn_2O_3 materials.

The synthesized mesoporous Mn_2O_3 materials were utilized as electroactive materials to evaluate the supercapacitor properties. The parameters for the supercapacitor with the synthesized mesoporous Mn_2O_3 electrode were determined by measuring the cyclicvoltametry (CV) at different scan rates in a 6 M KOH electrolyte. Figure 7a shows a series of CV curves of the synthesized mesoporous Mn_2O_3 electrode at different scan rates in a 6 M KOH electrolyte. Generally, in an electrochemical reaction, the conversion from Mn^{3+} to Mn^{4+} in an Mn_2O_3 electrode occurs via an oxidation reaction. This oxidation reaction normally accelerates the reaction kinetics of OH^- over the Mn_2O_3 cubic lattice through the chemisorbed and/or intercalated. The charge/discharge process can be explained by the following electrochemical reaction, which involves the chemisorption/intercalation of HO^- over the Mn_2O_3 surfaces:

$$Mn_2O_3 \ + \ HO^- \ \underset{\text{Dischage}}{\overset{\text{Charge}}{\rightleftarrows}} \ Mn^{4+}\,[Mn^{3+}]OH^-O_3 + \bar{e}$$
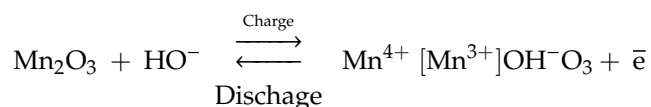
The prepared Mn_2O_3 electrode depicts the oxidation-reduction pair peaks with different curve shapes of the charge–discharge curves in relation to the variation in the scan rates. The observations principally suggest the origin of the faradaic pseudo-capacitance in an alkaline electrolyte over the surface of an Mn_2O_3 electrode. Moreover, the well-defined oxidation reduction pair within 0–1 V can also be ascribed to a faradaic redox reaction [40,41]. The plot of the capacitance versus the scan

rate for a fabricated pseudosupercapacitor based on a mesoporous Mn_2O_3 electrode is displayed in Figure 7b. In general, the specific capacitance (C_{sp}) is estimated from the CV curves using the following equation [42]:

$$C_{sp} = \frac{1}{mv(V_2 - V_1)} \int_{V_1}^{V_2} I(V)dV \tag{2}$$

where C_{sp} is the specific capacitance ($F \cdot g^{-1}$), I is the current (A), v is the scan rate, m is the mass of the active material (g) and ΔV is the potential range (V). As seen in Figure 7b, the fabricated pseudosupercapacitor based on the mesoporous Mn_2O_3 electrode exhibits a high C_{sp} of ~460 $F \cdot g^{-1}$ at a scan rate of 10 $mV \cdot s^{-1}$. This might be explained by the fact that there is an improvement of the surface area, the porous surface and uniformity, which might favor the generation of large active sites [43,44] and fast ionic transport over the surface of the Mn_2O_3 electrode. Specifically, the porous structure could provide a large and accessible surface area to ion adsorption, improve the accessibility of cations and shorten the ion diffusion path. The stability of the mesoporous Mn_2O_3 electrode is explored by observing the multicycle CV measurements in a 6 M KOH electrolyte. From Figure 7c, the slight shift in the oxidation peaks expresses the good stability of the mesoporous Mn_2O_3 electrode in the alkaline electrolyte. It is also seen that the anodic current in the Mn_2O_3 electrode is positively shifted with the increase, while the cathodic current is negatively shifted due to the increment in the electrical polarization and the fast and irreversible reactions as the scan rates increase. Here, the fast, irreversible reactions after 25 cycles might result from the accumulation of Mn^{4+} ions in the electrochemical system. The stability of the fabricated pseudosupercapacitor based on a mesoporous Mn_2O_3 electrode is shown in Figure 7d by measuring the capacitance after 5000 cycles. From Figure 7d, after 5000 cycles, the electrochemical system shows a reasonably high stability by retaining 83% of the initial capacity. Furthermore, the inset of Figure 7d presents the FESEM image of the mesoporous Mn_2O_3 electrode after 5000 cycles. The morphology of the Mn_2O_3 materials is not altered, except for an aggregation of small particles after cycling, suggesting the stability of the Mn_2O_3 electrode in the alkaline electrolyte. Hence, the reproducibility of a pseudosupercapacitor based on a mesoporous Mn_2O_3 electrode in a KOH electrolyte is remarkable and implies the low dissolution of the electro-active materials in a strong alkaline electrolyte after an electrochemical process.

　　The electrochemical Impedance Spectroscopy (EIS) for the fabricated pseudosupercapacitor based on the synthesized mesoporous Mn_2O_3 electrode was conducted to understand the electrochemical and electrical properties. Figure 8 shows the EIS plot, which was measured in the frequency range of 0.1–10^5 Hz. In the illustration of the equivalent circuit, the starting point in the Nyquist plot at a high-frequency region and the starting point at a low-frequency region represent the series resistance (R_s) and the charge transfer resistance (R_{ct}) of the electrode/electrolyte interface, respectively. C_{dl}, W and C_{pseudo} explain the double layer capacitance that arose by the parallel connection to R_{ct}, the Warburg diffusion element and the Faradaic capacitance generated by the contribution of the Mn_2O_3 electrode. As shown in Figure 8, the pseudosupercapacitor based on the synthesized mesoporous Mn_2O_3 electrode features a large phase angle near the low-frequency region, indicating the faradic capacitance behavior of the electrode. Importantly, in the EIS plot, the straight line in the low-frequency region, and the absence of any small semicircle in the high-frequency region, are indicative of the good capacitive nature of the present electrochemical system based on a mesoporous Mn_2O_3 electrode. Likewise, the observed straight line at a low frequency might reduce the diffusion length and accelerate the ions transportation on the mesoporous surface of the Mn_2O_3 electrode, as evidenced by the CV results.
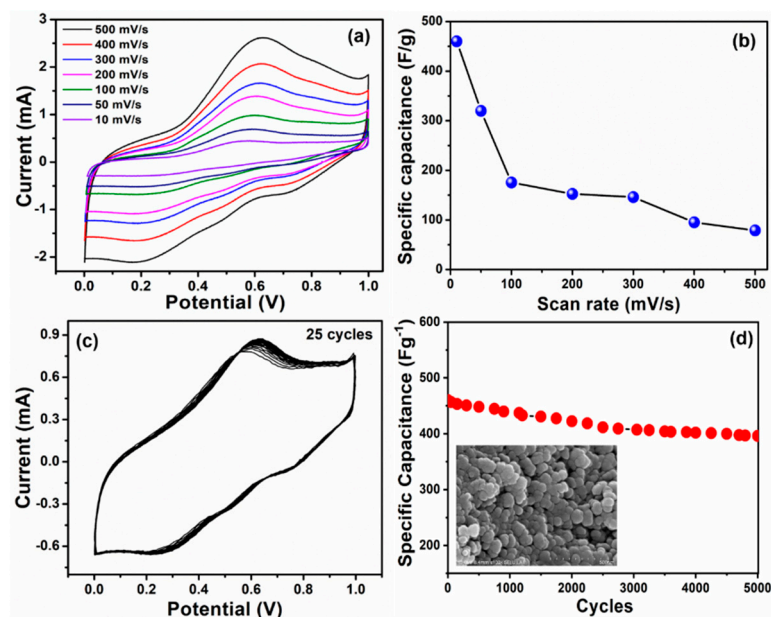
Figure 7. The (**a**) CV curves and (**b**) specific capacitance of the synthesized mesoporous Mn_2O_3 electrode at different scan rates ranging from 10 to 500 mV·s^{-1}, (**c**) multicycles CV curves and (**d**) variation in the specific capacitance of the synthesized mesoporous Mn_2O_3 electrode after 5000 cycles. The inset shows the FESEM image of the synthesized mesoporous Mn_2O_3 electrode after 5000 cycles.
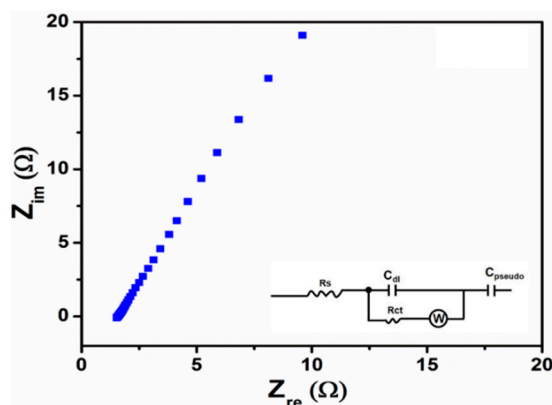

Figure 8. The EIS plot of the synthesized mesoporous Mn_2O_3 electrode at the Z_{im} versus the Z_{re} mode. The inset shows its corresponding equivalent circuit.

4. Conclusions

In summary, a facial hydrothermal process was adopted to synthesize well-crystalline mesoporous Mn_2O_3 materials for the fabrication of a pseudocapacitor. The crystalline and structural characterizations confirmed the formation of Mn_2O_3 materials without displaying any other oxide forms. The surface properties were analyzed, showing the mesoporous nature of Mn_2O_3 materials and an estimated high surface area of 76.9 m^2·g^{-1} with a good pore distribution. The fabricated pseudo-capacitor based on a Mn_2O_3 mesoporous particle electrode shows a reasonably high specific capacitance of ~460 F·g^{-1} at 10 mV·s^{-1} in a 6 M KOH aqueous solution. The enhancement in the capacitive properties might be attributed to the high surface area, porous surface and uniformity of the unique mesoporous particles morphology, resulting in the large generation of active sites and a fast ionic transport over the surface of the Mn_2O_3 electrode.

Author Contributions: Conceptualization, Y.-H.S., P.T.M.B., M.S.A., H.-R.L., D.K.S. and O-B.Y.; methodology, Y.-H.S., P.T.M.B., M.S.A., H.-R.L. and D.K.S.; software, Y.-H.S. and P.T.M.B.; validation, P.T.M.B., M.S.A., H.-R.L. and D.K.S.; formal analysis, Y.-H.S. and P.T.M.B.; investigation, Y.-H.S. and P.T.M.B.; resources, Y.-H.S. and P.T.M.B.;

References

1. Miller, J.R.; Simon, P. Electrochemical capacitors for energy management. *Science* **2008**, *321*, 651–652. [CrossRef] [PubMed]
2. Simon, P.; Gogotsi, Y. Materials for electrochemical capacitors. *Nat. Mater.* **2008**, *7*, 845–854. [CrossRef]
3. Wei, D.; Scherer, M.R.; Bower, C.; Andrew, P.; Ryhanen, T.; Steiner, U. A nanostructured electrochromic supercapacitor. *Nano Lett.* **2012**, *12*, 1857–1862. [CrossRef] [PubMed]
4. Yuan, C.Z.; Wu, H.B.; Xie, Y.; Lou, X.W. Mixed transition-metal oxides: Design, synthesis, and energy-related applications. *Angew. Chem. Int. Ed.* **2014**, *53*, 1488–1504. [CrossRef] [PubMed]
5. Jiang, H.; Li, C.; Ma, J. Polyaniline–MnO_2 coaxial nanofiber with hierarchical structure for high-performance supercapacitors. *J. Mater. Chem.* **2012**, *22*, 2751. [CrossRef]
6. Devaraj, S.; Munichandraiah, N. High capacitance of electrodeposited MnO_2 by the effect of a surface-active agent. *Electrochem. Solid State Lett.* **2005**, *8*, 373–377. [CrossRef]
7. Zhao, D.; Tian, J.S.; Ji, Q.Q.; Zhang, J.T.; Zhao, X.S.; Guo, P.Z. Mn_2O_3 nanomaterials: Facile synthesis and electrochemical properties. *Chin. J. Inorg. Chem.* **2010**, *26*, 832–838.
8. Jang, G.; Ameen, S.; Akhtar, M.S.; Kim, E.-B.; Shin, H.S. Electrochemical Investigations of Hydrothermally Synthesized Porous Cobalt Oxide (Co3O4) Nanorods: Supercapacitor Application. *ChemistrySelect* **2017**, *2*, 8941–8949. [CrossRef]
9. Li, Z.Y.; Bui, P.T.M.; Kwak, D.H.; Akhtar, M.S.; Yang, O.B. Enhanced electrochemical activity of low temperature solution process synthesized Co_3O_4 nanoparticles for pseudo-supercapacitors applications. *Ceram. Int.* **2016**, *42*, 1879–1885. [CrossRef]
10. Li, Z.Y.; Akhtar, M.S.; Yang, O.B. Supercapacitors with ultrahigh energy density based on mesoporous carbon nanofibers: Enhanced double-layer electrochemical properties. *J. Alloy. Compd.* **2015**, *653*, 212–218. [CrossRef]
11. Seo, M.K.; Saouab, A.; Park, S.J. Effect of annealing temperature on electrochemical characteristics of ruthenium oxide/multi-walled carbon nanotube composites. *Mater. Sci. Eng. B* **2010**, *167*, 65–69. [CrossRef]
12. Shambharkar, B.H.; Umare, S.S. Production and characterization of polyaniline/Co_3O_4 nanocomposite as a cathode of Zn–polyaniline battery. *Mater. Sci. Eng. B* **2010**, *175*, 120–128. [CrossRef]
13. Zheng, Z.; Huang, L.; Zhou, Y.; Hu, X.W.; Ni, X.M. Large-scale synthesis of mesoporous CoO-doped NiO hexagonal nanoplatelets with improved electrochemical performance. *Solid State Sci.* **2009**, *11*, 1439–1443. [CrossRef]
14. Prasad, K.R.; Miura, N. Electrochemical synthesis and characterization of nanostructured tin oxide for electrochemical redox supercapacitors. *Electrochem. Commun.* **2004**, *6*, 849–852. [CrossRef]
15. Jiang, H.; Zhao, T.; Ma, J.; Yan, C.; Li, C. Ultrafine manganese dioxide nanowire network for high-performance supercapacitors. *Chem. Commun.* **2011**, *47*, 1264. [CrossRef] [PubMed]
16. Rakhi, R.B.; Chen, W.; Cha, D.; Alshareef, H.N. Substrate dependent self-organization of mesoporous cobalt oxide nanowires with remarkable pseudocapacitance. *Nano Lett.* **2012**, *12*, 2559. [CrossRef] [PubMed]
17. Lu, Q.; Lattanzi, M.W.; Chen, Y.; Kou, X.; Li, W.; Fan, X.; Unruh, K.M.; Chen, J.G.; Xiao, J.Q. Supercapacitor electrodes with high-energy and power densities prepared from monolithic NiO/Ni nanocomposites. *Angew. Chem.* **2011**, *50*, 6847–6850. [CrossRef]
18. Benson, J.; Boukhalfa, S.; Magasinski, A.; Kvit, A.; Yushin, G. Chemical vapor deposition of aluminum nanowires on metal substrates for electrical energy storage applications. *ACS Nano* **2012**, *6*, 118–125. [CrossRef]
19. Xie, K.; Li, J.; Lai, Y.; Lu, W.; Zhang, Z.; Liu, Y.; Zhou, L.; Huang, H. Highly ordered iron oxide nanotube arrays as electrodes for electrochemical energy storage. *Electrochem. Commun.* **2011**, *13*, 657–660. [CrossRef]

20. Ghosh, S.; Polaki, S.R.; Sahoob, G.; Jin, E.-M.; Kamruddin, M.; Cho, J.S.; Jeong, S.M. Designing metal oxide-vertical graphene nanosheets structures for 2.6 V aqueous asymmetric electrochemical capacitor. *J. Ind. Eng. Chem.* **2019**, *72*, 107–116. [CrossRef]

21. Nagamuthu, S.; Ryu, K.-S. MOF-derived microstructural interconnected network porous Mn_2O_3/C as negative electrode material for asymmetric supercapacitor device. *CrystEngComm* **2019**, *21*, 1442–1451. [CrossRef]

22. Sui, N.; Duan, Y.; Jiao, X.; Chen, D. Large-scale preparation and catalytic properties of one-dimensional α/β-MnO_2 nanostructures. *J. Phys. Chem. C* **2009**, *113*, 8560–8565. [CrossRef]

23. Kolathodi, M.S.; Rao, S.N.H.; Natarajana, T.S.; Singh, G. Beaded manganese oxide (Mn_2O_3) nanofibers: Preparation and application for capacitive energy storage. *J. Mater. Chem. A* **2016**, *4*, 7883–7891. [CrossRef]

24. Nakayama, M.; Tanaka, A.; Sato, Y.; Tonosaki, T.; Ogura, K. Electrodeposition of manganese and molybdenum mixed oxide thin films and their charge storage properties. *Langmuir* **2005**, *21*, 5907. [CrossRef]

25. Wu, Z.-S.; Ren, W.; Wang, D.-W.; Li, F.; Liu, B. High-energy MnO_2 nanowire/graphene and graphene asymmetric electrochemical capacitors. *ACS Nano* **2010**, *4*, 5835–5842. [CrossRef]

26. Fischer, A.E.; Pettigrew, K.A.; Rolison, D.R.; Stroud, R.M.; Long, J.W. Incorporation of homogeneous, nanoscale MnO_2 within ultraporous carbon structures via self-limiting electroless deposition: Implications for electrochemical capacitors. *Nano Lett.* **2007**, *7*, 281–286. [CrossRef]

27. Ghodbane, O.; Pascal, J.-L.; Favier, F. Microstructural effects on charge-storage properties in MnO_2-based electrochemical supercapacitors. *ACS Appl. Mater. Interfaces* **2009**, *1*, 1130–1139. [CrossRef]

28. Zhi, M.; Xiang, C.; Li, J.; Li, M.; Wu, N. Nanostructured carbon–metal oxide composite electrodes for supercapacitors: A review. *Nanoscale* **2013**, *5*, 72–88. [CrossRef]

29. Jiang, J.; Li, Y.; Liu, J.; Huang, X.; Yuan, C.; Lou, X.W. Recent advances in metal oxide-based electrode architecture design for electrochemical energy storage. *Adv. Mater.* **2012**, *24*, 5166–5180. [CrossRef]

30. Han, Z.J.; Seo, D.H.; Yick, S.; Chen, J.H.; Ostrikov, K. MnOx/carbon nanotube/reduced graphene oxide nanohybrids as high-performance supercapacitor electrodes. *NPG Asia Mater.* **2014**, *6*, e140. [CrossRef]

31. Demir, M.; Ashourirad, B.; Mugumya, J.H.; Saraswata, S.K.; El-Kaderi, H.M.; Gupta, R.B. Nitrogen and oxygen dual-doped porous carbons prepared from pea protein as electrode materials for high performance supercapacitors. *Int. J. Hydrog. Energy* **2018**, *43*, 18549–18558. [CrossRef]

32. Cheng, F.; Shen, J.; Ji, W.; Tao, Z.; Chen, J. Selective synthesis of manganese oxide nanostructures for electrocatalytic oxygen reduction. *ACS Appl. Mater. Interfaces* **2009**, *1*, 460–466. [CrossRef] [PubMed]

33. Jenkins, R. *Introduction to X-Ray Powder Diffractometry*; John Wiley & Sons, Inc.: New York, NY, USA, 1996; p. 90.

34. Gillot, B.; El Guendouzi, M.; Laarj, M. Particle size effects on the oxidation–reduction behavior of Mn_3O_4 hausmannite. *Mater. Chem. Phys.* **2001**, *70*, 54–60. [CrossRef]

35. Chen, Z.W.; Lai, J.K.L.; Shek, C.H. Influence of grain size on the vibrational properties in Mn_2O_3 nanocrystals. *J. Non Cryst. Solids* **2006**, *352*, 3285–3289. [CrossRef]

36. Han, Y.-F.; Ramesh, K.; Chen, L.; Widjaja, E.; Chilukoti, S.; Chen, F. Controlled synthesis, characterization, and catalytic properties of Mn2O3 and Mn3O4 nanoparticles supported on mesoporous silica SBA-15. *J. Phys. Chem. B* **2007**, *111*, 2830–2833.

37. Zhang, Y.; Yan, Y.; Wang, X.; Li, G.; Deng, D.; Jiang, L.; Shu, C.; Wang, C. Facile synthesis of porous Mn_2O_3 nanoplates and their electrochemical behavior as anode materials for lithium ion batteries. *Chem. A Eur. J.* **2014**, *20*, 6126–6130. [CrossRef]

38. Jahan, M.; Tominaka, S.; Henzie, J. Phase pure α-Mn_2O_3 prisms and their bifunctional electrocatalytic activity in oxygen evolution and reduction reactions. *Dalton Trans.* **2016**, *45*, 18494–18501. [CrossRef]

39. Ilton, E.S.; Post, J.E.; Heaney, P.J.; Ling, F.T.; Kerisit, S.N. XPS determination of Mn oxidation states in Mn (hydr)oxides. *Appl. Surf. Sci.* **2016**, *366*, 475–485. [CrossRef]

40. Toupin, M.; Brousse, T.; Bélanger, D. Influence of microstucture on the charge storage properties of chemically synthesized manganese dioxide. *Chem. Mater.* **2002**, *14*, 3946–3952. [CrossRef]

41. Toupin, M.; Brousse, T.; Bélanger, D. Charge storage mechanism of MnO_2 electrode used in aqueous electrochemical capacitor. *Chem. Mater.* **2004**, *16*, 3184–3190. [CrossRef]

42. Rajkumar, M.; Hsu, C.-T.; Wu, T.-H.; Chen, M.-G.; Hu, C.-C. Advanced materials for aqueous supercapacitors in the asymmetric design. *Prog. Nat. Sci. Mater. Int.* **2015**, *25*, 527. [CrossRef]

43. Gopalakrishnan, I.K.; Bagkar, N.; Ganguly, R.; Kulshreshtha, S.K. Synthesis of superparamagnetic Mn_3O_4 nanocrystallites by ultrasonic irradiation. *J. Cryst. Growth* **2005**, *280*, 436. [CrossRef]
44. Li, Z.-Y.; Akhtar, M.S.; Bui, P.T.M.; Yang, O.-B. Predominance of two dimensional (2D) Mn_2O_3 nanowalls thin film for high performance electrochemical supercapacitors. *Chem. Eng. J.* **2017**, *330*, 1240–1247. [CrossRef]